Manifold-Based Nonlocal Second-Order Regularization for Hyperspectral Image Inpainting

Jianwei Zheng , Jiawei Jiang , Honghui Xu, Zhi Liu , and Fei Gao

Abstract—The low-dimensional manifold of image patches has been introduced as regularizer term, and shown effective in hyperspectral image inpainting. However, in this article, we find that using only the low-dimensional property of manifold may not always generate smooth results. In terms of this, we first present a higher order term to the low-dimensional manifold model, namely nonlocal second-order regularization (NSR), which provides better approximation to the real data distribution and manifests both the properties of low dimensionality and smoothness. Moreover, in order to balance the known and unknown sets, we further propose a weighted version of NSR, called WNSR. The generalized minimal residual algorithm is adopted to solve this unsymmetrical model, in which a semi-patch is applied for acceleration of the nearest neighbor search. Finally, we conduct intensive numerical experiments on five well-known datasets to verify the superiority of our method. The inpainting results show that our proposed (W)NSR significantly outperforms the state-of-the-art methods with respect to both visual and numerical quality.

Index Terms—Hyperspectral image (HSI) inpainting, manifold model, patch-based method, second-order regularization, weighted nonlocal method.

I. Introduction

HYPERSPECTRAL images (HSIs) are acquired with imaging spectrometer under continuous and narrow spectral bands, which results in rich details of object surface reflectance across quite a huge amount of bands ranging from the visible wavelength to the sub-infrared one. Therefore, HSIs have been widely studied and applied in the remote sensing domain [1]–[3], including urban layout, military surveillance, mineral exploration, and environmental monitoring, to just name a few. Nevertheless, the practical potential is usually compromised since the rich spectral information comes at the cost of greatly restricting the spatial resolutions. Besides, some of the pixels might be missing due to the malfunctions of the collecting devices or certain atmospherical occlusions, resulting in incomplete observations of the target area [4]. Therefore, an essential task in hyperspectral analysis is to recover the original image from the incomplete observations. In this work, we mainly focus on the missing pixel recovery, which is termed as HSI inpainting and is typically an ill-posed inverse problem. Generally speaking, there are two mainstream methods to solve this problem, i.e., the data-driven scheme and the knowledge-driven scheme. The former is dominated by the well-known deep learning-based methods, which enjoy high popularity due to their strong power on nonlinear learning capabilities. In practice, several network architectures, such as convolutional neural nets [5], [6] and generative adversarial nets [7], have been successfully extended to the field of HSI reconstruction. However, although excellent performance can be achieved, deep learning-based methods suffer from two drawbacks that hinder its usage in singleton inpainting problem, especially in noncommercial home computers. On one hand, a large amount of training time and training data are required for optimization of massive network parameters. Correspondingly, the requirements for hardware are comparatively high. On the other hand, in the image inpainting field, the performance of most methods based on deep learning are quite sensitive to different missing types and missing rates. In this work, we focus on the knowledge-driven scheme for inpainting single HSI without any auxiliary images and pretrained models, where appropriate prior properties of the latent HSI are necessitated to steer the recovery problem and shrink the solution space.

Mathematically, a knowledge-based HSI restoration problem can be considered as recovering the clean counterpart f from a degraded image b based on the degradation operator $\Phi(f) = b$ and certain prior knowledge $h(f)$. Note that the equivalence in the degradation process may not strictly hold, hence the general framework of HSI inpainting is always relaxed as follows:

$$\min \lambda \parallel b - \Phi(f) \parallel_2^2 + h(f). \tag{1}$$

The first term in (1) is the loss measuring the fidelity of the reconstructed image to the input image with known samples, whose contribution is controlled by the tradeoff parameter λ. The prior information $h(f)$, such as piecewise smoothness, shape edges, textures, and repetitive patterns, makes regularization method (1) quite effective to tackle real-world HSI analysis problems.

Low-rank matrix approximation is one of the most popular regularizers in HSI processing. For a clean HSI data, it is usually assumed that each of its pixels can be linearly composed of a few

The authors are with the School of Computer Science and Engineering, Zhejiang University of Technology, Hangzhou 310014, China (e-mail: zjw@zjut.edu.cn; jjw_zjut@163.com; xhh@zjut.edu.cn; lzhi@zjut.edu.cn; feig@zjut.edu.cn).

endmembers. On that basis, the low-rank matrix factorization [8]–[10] has been introduced to capture the core structure of the HSI. However, the matricization techniques should preliminarily vectorize all HSI bands, which inevitably loses the original structural information to some extent. In order to better maintain the spatial–spectral structure, different low-rank-based tensor approximation frameworks are developed in recent years [11], [12]. For instance, Lu *et al.* proposed a tensor robust principal component analysis (TRPCA) [13] method and defined a new tensor nuclear norm (TNN) [14] as the tightest convex surrogate of tensor rank. However, while both TRPCA and TNN can achieve appealing performance in image inpainting, they suffer from the per-iteration computational cost due to the necessity of singular value decomposition. To improve per-iteration efficiency and avoid out-of-memory errors, several low-rank tensor factorization schemes have been introduced to describe the HSI low-rank property, including Tucker [15], [16], tensor train [17], and tensor ring [10], [18], etc.

As presented in [19], only the low-rank property may be not sufficient to cover the prior spatial information. Moreover, aforementioned algorithms mainly aim to recover the global structure, but neglect to capture the local or nonlocal information of the observed image. Accordingly, in the past decades, patch-based techniques, such as nonlocal means [20] and two-stage low-rank approximation [21], have been successfully applied to HSI inpainting or other image processing tasks. These methods focus on using the information of internal and external patches, with the truth that similarity between pixels can be measured by l_2 distance among their neighbors or the patches containing them. The efficacy of the patch-based algorithm stems from the nonlinear and self-similar structures in the spatial domain of HSI patches, which can build highly data-adaptive representations. Together with adaptive thresholding, these structures can be closely connected to typical total variation approaches [22]. Recently, a variant of the patch-based algorithm, i.e., manifold models, has attracted increased popularity due to its valuable insight in the construction of new HSI processing model. It hypothesizes that the patches are likely to concentrate around low-dimensional nonlinear manifolds [23], [24]. From the viewpoint of diffusion geometry [25], [26], the nonlocal mean filter can also be interpreted as a diffusion process on the patch manifold.

Based on the low-dimensional characteristic of patch manifold, two new approaches named as low-dimensional manifold model (LDMM) [27] and weighted nonlocal Laplacian (WNLL) [28] are proposed with strong results. Both of these penalize a direct regularization on the dimension of patch manifold and present a variational argument for patch-based image processing. Following this line, Zhu *et al.* [29] successfully extends the LDMM model to HSI inpainting problem. Based on these three works, this article is motivated by the wish to better exploit the low-dimensional structure of the manifold. Specifically, we find that only using the first-order LDMM regularizer does not guarantee the smoothness of the reconstructed patch groups. For instance, Fig. 1 shows two degraded interpolations in red circles. One can observer that though the interpolated surface follows a low-dimensional manifold, these two points clearly violate
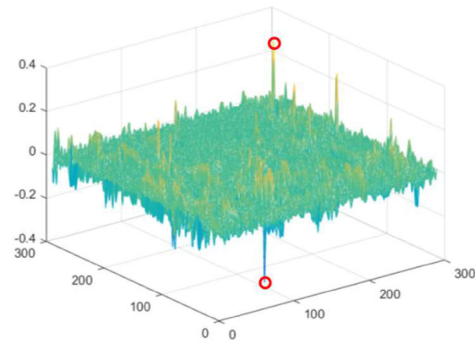

Fig. 1. Degraded low-dimensional surface without using high-order regularization.

the smooth interpolation. To remedy this issue, we attempt to combine both the properties of low dimensionality and smoothness together. Accordingly, a new method, namely nonlocal second-order regularization (NSR) constrained HSI inpainting, is proposed. Note that the scheme of introducing higher-order regularization terms has already been proposed in the image analysis [30]. However, as far as we know, this is the first to penalize second-order constraint into HSI inpainting. Moreover, motivated by the WNLL scheme, we further present a weighted nonlocal second-order regularization (WNSR), which can significantly improve the recovery performance of the nonweighted counterpart. Concretely, our contributions are threefold.

1) We add a second-order constraint based on the low-dimensional manifold to ensure the smoothness of the reconstructed HSIs and make the interpolation more reasonable. Moreover, we develop the proposed second-order regularization in the weighted nonlocal mode for relieving the interpolation fluctuations when the proportion of known pixels to unknown pixels is extremely low.

2) Generally, huge memory storage is required to apply (W)NSR regularizer in high-dimensional data. Due to the fact that HSI is a collection of many 2-D images with the same spatial location, we treat all spectral bands separately to reduce the computational cost. Moreover, the semi-local patch operation can be optionally introduced into our model, which speeds up the nearest neighbor search and improves the running efficiency.

3) We successfully apply the manifold-based nonlocal second-order regularization to HSI inpainting. The experimental results in various situations demonstrate that, compared with other algorithms, our method can achieve excellent performance with comparable runtime. It is worth mentioning that WNSR can still generate desirable visual quality under very severe missing rates, such as 95%.

The remainder of this article is outlined as follows. A review of the low-dimensional manifold model is introduced in Section II. Section III illustrates the proposed (W)NSR method and the corresponding optimization algorithm. Different experiments and results are shown in Section IV. The final section concludes this article.

II. PATCH-BASED LOW-DIMENSIONAL MANIFOLD REGULARIZATION

To harvest the manifold property of HSI data, the work in [29] directly adopts LDMM as a constraint, which utilizes the dimension of patch manifold as the regularization to recover the incomplete images. In this section, we will briefly introduce the basic idea of LDMM for self-containedness.

A. Patch Manifold

Assume $f \in \mathbf{R}^{m \times n \times B}$ be a given HSI, where m, n, B denote the width, height, and spectral length, respectively. For any spatial coordinate $x \in \bar{H} := [m] \times [n]$, where $[m] = \{1, 2, \ldots, m\}$, we can define a patch $\mathcal{P}f(\mathbf{x})$ as a 3-D cubic of size $s_1 \times s_2 \times s_3$ from the original data f, and x be the pixel in the top-left of the $s_1 \times s_2$-sized patch. The overall patch set $\mathcal{P}(f)$ can then be defined as the assembly of all patches

$$\mathcal{P}(f) = \{\mathcal{P}f(x) : x \in \bar{H}\} \in \mathbf{R}^d, d = s_1 \times s_2 \times s_3. \quad (2)$$

The point cloud set $\mathcal{P}(f)$ is usually related to a stack of low-dimensional manifold embedded in $\mathbf{R}^d$ [27], which is called *patch manifold* in accordance with f and denoted as $\mathcal{M}(f)$. According to [29], the underlying manifold $\mathcal{M}(f)$ can be approximated by a $3K$ dimensional manifold, where K is the endmember number that can generate the entire HSI. Typically, K is much smaller than d.

One point deserves to remark is that the choice of the patch size $s_1 \times s_2 \times s_3$ shall be varied in practice. Normally s_1 and s_2 are chosen corresponding to the spatial resolution of the HSI, s_3 in this article is fixed as B, which is the spectral number of the HSI. Of course, sometimes it can be smaller according to the in-hand problems. In the sequel, we denote $\mathcal{P}$ as a projection operator: $\mathbf{R}^{m \times n \times B} \rightarrow \mathbf{R}^{d \times |m \times n|}$, which maps any HSI $f \in \mathbf{R}^{m \times n \times B}$ to the patch set $\mathcal{P}(f) \in \mathbf{R}^{d \times |m \times n|}$.

B. Low-Dimensional Manifold Regularization

Based on the definition in Section II-A, the dimension of the patch manifold can be used as a regularization in HSI image processing. Suppose $C = \{c_1, c_2, \ldots, c_n\}$ is the complete set of points in $\mathbf{R}^d$, and $V = \{v_1, v_2, \ldots, v_n\}$ is the observed subset of C, i.e., $V \subset C$. Let g defined as an indicator function on subset V, the inpainting problem is to extend b to C by finding a smooth function u on manifold $\mathcal{M}$ that are consistent with g when the index lies in subset V. In the implementation, LDMM adopts a Dirichlet energy to regularize the dimension of $\mathcal{M}$, that is

$$\text{LDMM}(u) = \frac{1}{2} \parallel \nabla_{\mathcal{M}} u \parallel_2^2 \quad (3)$$

where $\nabla_{\mathcal{M}} u$ denotes the gradient of u on manifold $\mathcal{M}$, $\parallel \cdot \parallel_2$ is the l_2 norm. In [27], Osher *et al.* rewrite the Dirichlet regularizer in a geometric manner and give a simple and explicit formula to calculate the dimension of smooth manifold as follows:

$$\dim(\mathcal{M}) = \sum_{l=1}^{d} |\nabla_{\mathcal{M}} \alpha_l(p)|^2 \quad (4)$$

where α_l, $l = (1, \ldots, d)$ are the coordinate functions on $\mathcal{M}$, i.e., $\alpha_l = u_l, \forall u = (p_1, \ldots, p_d) \in \mathcal{M}$.

The regularizer in (4) is actually the l_1 norm of local dimension over the patch manifold. This is beneficial for the hyperspectral reconstruction problem. First, patch manifold $\mathcal{M}$ is not all globally smooth so that taking the summation of all local dimensions of $\mathcal{M}$ can address the piecewise smooth situation. Second, there may be some unmixed materials in the HSI, which means $\mathcal{M}$ has zero local dimension in these elements, which implies adopting the l_1 norm can promote sparsity and correctly adhere to this prior knowledge. With constraint $u(v) = g(v), \forall v \in V$, one can recover the missing part from minimizing the Dirichlet energy. Recall that g denotes the observed part of u, and $V \in C$ denotes the labeled pixels.

III. NONLOCAL SECOND-ORDER REGULARIZER FOR HSI INPAINTING

A. Nonlocal Second-Order Regularizer

As stated in the Introduction section, we attempt to explore a better interpolation by assuming not only the low dimensional manifold but also the smoothness. For this purpose, in addition to the LDMM regularizer, a nonlocal second-order regularization is also considered. The NSR term reads as follows:

$$\text{NSR}(u) := \text{LDMM}(u) + \frac{\beta}{2} \int_{\mathcal{M}} (\Delta_{\mathcal{M}} u)^2. \quad (5)$$

Note that the first term in (5) can be simplified as (4). However, this would result in an asymmetrical formulation in the optimization step, which further slows the convergence of the algorithm. Following the second approach in [29], one can approximate the energy $\nabla_{\mathcal{M}} u$ in the discrete setting using a nonlocal gradient

$$\nabla_{\mathcal{M}} u(p, q) \approx \sqrt{w(p, q)}(u(q) - u(p)) := \nabla_C u(p, q)$$
$$p, q \in C \subset \mathcal{M} \quad (6)$$

where p, q is a set of point cloud on the patch manifold $\mathcal{M}$, $w(p, q)$ is a weight function which usually obtained as $w(p, q) = \exp(-\frac{\parallel p-q \parallel^2}{\sigma^2})$ with σ being a normalizing parameter. Then, the first term in (5) can be formulated as follows:

$$\text{LDMM}(u) \approx \frac{1}{2} \sum_{p,q \in C} w(p, q)(u(p) - u(q))^2 = \parallel \nabla_C u \parallel_2^2. \quad (7)$$

The negative of the first variation of (7) reads as follows:

$$-\partial_u(\parallel \nabla_C u \parallel_2^2) = \sum_{q \in C} w(p, q)(u(p) - u(q)). \quad (8)$$

Such transformation is the nonlocal Laplacian method that has been widely used in image processing [31], [32], which can also be called graph Laplacian and behaves as the discrete approximation to the second term in (5). We denote it as GL to simplify the notation

$$\text{GL}(u) = \sum_{q \in C} w(p, q)(u(p) - u(q)). \quad (9)$$

Taking (9) together with (7) leads to the specific NSR regularization in the discrete setting

$$\text{NSR}(u) := \min_u \parallel \nabla_C u \parallel_2^2 + \frac{\beta}{2} \parallel \text{GL}(u) \parallel_2^2 . \qquad (10)$$

In [28], the technique of WNLL is proposed to balance the known and unknown pixels and meanwhile hold the symmetry of the subsequent formulations. The WNLL operation can be simply written as follows:

$$\text{WNLL} := \parallel \nabla_{\mathcal{M}} u_{|C \setminus V} \parallel_2^2 + \frac{|C|}{|V|} \parallel \nabla_{\mathcal{M}} u_{|V} \parallel_2^2 \qquad (11)$$

where

$$\parallel \nabla_{\mathcal{M}} u_{|V} \parallel_2^2 = \frac{1}{2} \sum_{p \in V, q \in C} w(p,q)(u(p) - u(q))^2. \qquad (12)$$

We omit the description of the second term $\parallel \nabla_{\mathcal{M}} u_{|C \setminus V} \parallel_2^2$ due to its similarity to the first term.

Using WNLL, the proposed NSR regularization can also be rewritten in a discrete setting. We term it as the WNSR

$$\text{WNSR}(u) := \min_u \frac{\beta}{2} \left[\parallel (\text{GL}u)_{|C \setminus V} \parallel_2^2 + \frac{|C|}{|V|} \parallel (\text{GL}u)_{|V} \parallel_2^2 \right] + \text{WNLL}(u) \qquad (13)$$

where

$$\parallel (\text{GL}u)_{|V} \parallel_2^2 = \sum_{p \in V} \left(\sum_{q \in C} w(p,q)(u(p) - u(q)) \right)^2 \qquad (14)$$

and $\parallel (\text{GL}u)_{|C \setminus V} \parallel_2^2$ follows a similar operation.

B. Semi-Local Patches

The previous work [28] has shown that adding local coordinates to the nonlocal patches can reduce the number of optimization iterations. This scheme is called semi-local patch and has been successfully applied to many image processing issues [33]. Following this operation, we replace the semi-local patch instead of the nonlocal patch by adding spatial information with a weight γ, i.e.

$$\mathcal{P}'(\boldsymbol{f}) = \{\mathcal{P}\boldsymbol{f}(x), \gamma x\} \in \mathbf{R}^{d+2}, d = s_1 \times s_2 \times B$$

where $x \in \bar{H} := \{1, 2, \dots, m\} \times \{1, 2, \dots, n\}$ is the index of this pixel. From the geometrical perspective, if γ tends to ∞, this parameterization is determined by local 2-D coordinate and typically bias to high curvature. In other words, the dimension of patch manifold must be very low. Conversely, if γ tends to 0, the latent patch manifold may own a higher dimension. However, the manifold may become smoother. The main effort lies in finding a proper compromise between the manifold dimension and the effect of the regularization. The detailed experiment about the choice of γ is presented in Section IV.

C. (W)NSR for Hyperspectral Inpainting

As for the HSI inpainting problems, the main objective is to recover the unknown HSI $\boldsymbol{f}$ from the incomplete data $\boldsymbol{b} \in \mathbf{R}^{m \times n \times B}$, $\boldsymbol{b}$ is only known on a random subset $H^t \in \bar{H}^t =$

$[m] \times [n]$, where t refers to some band number. In the sequel, we directly discuss the model details for WNSR. NSR can be easily obtained since it is a special case of WNSR by setting all weights to 1. Recall that the point cloud $\mathcal{P}\boldsymbol{f}(x)$ and the initial cost function of WNSR, when used in HSI inpainting, can be formulated as follows:

$$\min_f \quad \text{WNLL}(\mathcal{P}(\boldsymbol{f})) + \frac{\beta}{2} \parallel \sqrt{D} \cdot GL(\mathcal{P}(\boldsymbol{f})) \parallel_2^2 \\ \text{s.t.} \quad \boldsymbol{f}(x) = \boldsymbol{b}(x) \qquad (15)$$

where β is the regularization parameter, $D = \text{diag}\{d_1, d_2, \dots d_{|\bar{H}|}\}$ with $d_j = 1$ for $x_j \in \bar{H}^t \setminus H^t$ and $d_j = \frac{|\bar{H}^t|}{|H^t|}$ for $x_j \in H^t$. GL is the $|C| \times |C|$ Laplacian matrix defined in (14). To specify the optimization procedure of WNSR, we further rewrite (15) as follows:

$$\min_f \sum_{i=1}^{d_s} \sum_{t=1}^{B} \left[\sum_{x \in \bar{H}^t \setminus H_i^t} \sum_{y \in \bar{H}^t} w(x,y)(\mathcal{P}_i^t \boldsymbol{f}(x) - \mathcal{P}_i^t \boldsymbol{f}(y))^2 \right. \\ \left. + \frac{|\bar{H}^t|}{|H^t|} \sum_{x \in H_i^t} \sum_{y \in \bar{H}^t} w(x,y)(\mathcal{P}_i^t \boldsymbol{f}(x) - \mathcal{P}_i^t \boldsymbol{f}(y))^2 \right] \\ + \lambda \sum_{t=1}^{B} \parallel \boldsymbol{f}^t - \boldsymbol{b}^t \parallel_2^2 + \sum_{i,t} \frac{\beta}{2} \parallel \sqrt{D} \cdot GL(\mathcal{P}_i^t \boldsymbol{f}) \parallel_2^2 \qquad (16)$$

where $d_s = s_1 \times s_2$ is the spatial size of the patches, $\mathcal{P}_i^t \boldsymbol{f}(x)$ is the ith spatial element of patch $\mathcal{P}^t \boldsymbol{f}(x)$ in band t. $\frac{|\bar{H}^t|}{|H^t|}$ is the inverse ratio of the sampling rate, x, y are the points in $\bar{H}$ or H_i^t, operator $\mathcal{P}_i$ satisfies $\mathcal{P}_i^t \boldsymbol{f}(x) = \mathcal{P}_i \boldsymbol{f}^t(x)$. Note that (16) can be decoupled with regard to the spectral number t for any given $t \in [B]$, it follows that

$$\min_{f^t} \sum_{i=1}^{d_s} \left[\sum_{x \in \bar{H} \setminus H_i^t} \sum_{y \in \bar{H}} w(x,y)(\mathcal{P}_i \boldsymbol{f}^t(x) - \mathcal{P}_i \boldsymbol{f}^t(y))^2 \right. \\ \left. + r \sum_{x \in H_i^t} \sum_{y \in \bar{H}} w(x,y)(\mathcal{P}_i \boldsymbol{f}^t(x) - \mathcal{P}_i \boldsymbol{f}^t(y))^2 \right] \\ + \lambda \parallel \boldsymbol{f}^t - \boldsymbol{b}^t \parallel_2^2 + \frac{\beta}{2} \sum_{i=1}^{d_s} \parallel \sqrt{D} \cdot GL(\mathcal{P}_i \boldsymbol{f}^t) \parallel_2^2, \\ t \in \{1, 2, \dots, B\} \qquad (17)$$

where $r = \frac{|\bar{H}^t|}{|H^t|}$, λ is the penalty parameter. Through a standard variational deduction, we can obtain a Euler–Lagrange-like equation from (17), i.e.

$$\mu \sum_{i=1}^{d_s} \mathcal{P}_i^* \mathcal{I}_{H_i^t} \mathcal{F}_i^t(x) + \sum_{i=1}^{d_s} \mathcal{P}_i^* \mathcal{G}_i^t(x) + \beta \mathcal{P}_i^* GL^T \cdot D \cdot GL(x) \\ + \lambda \mathcal{I}_{H^t}(\boldsymbol{f}^t - \boldsymbol{b}^t)(x) = 0, \forall x \in \bar{H} \qquad (18)$$

where we denote $\mu = r - 1$ for simplicity, $\mathcal{P}_i^*$ is the adjoint operator of $\mathcal{P}_i$, $\mathcal{I}_{H^t}$ is the projection operator mapping $\boldsymbol{f}^t(x)$ to 0 when $x \notin H^t$, that is

$$\mathcal{I}_{H^t} \boldsymbol{f}^t(x) = \begin{cases} \boldsymbol{f}^t(x) & x \in H^t \\ 0 & x \notin H^t \end{cases} \qquad (19)$$

and

$$\begin{cases} GL = \mathcal{F}_i^t(x) = \sum_{y \in \bar{H}} w(x,y) \left(\mathcal{P}_i \boldsymbol{f}^t(x) - \mathcal{P}_i \boldsymbol{f}^t(y) \right) \\ \mathcal{G}_i^t(x) = \sum_{y \in \bar{H}} 2w(x,y) \left(\mathcal{P}_i \boldsymbol{f}^t(x) - \mathcal{P}_i \boldsymbol{f}^t(y) \right) \\ + \mu \sum_{y \in H_i^t} w(x,y) \left(\mathcal{P}_i \boldsymbol{f}^t(x) - \mathcal{P}_i \boldsymbol{f}^t(y) \right). \end{cases} \tag{20}$$

The symbol $x_{\hat{i}}$ is used to denote the ith spatial pixel after x in the same patch. The trick of periodic padding would be used in the case that when the index exceeds the boundary of the spatial domain. With all these settings, we can easily obtain

$$\begin{cases} \mathcal{P}_i \boldsymbol{f}^t(x) = \boldsymbol{f}^t(x_{\widehat{i-1}}) \\ \mathcal{P}_i^* \boldsymbol{f}^t(x) = \boldsymbol{f}^t(x_{\widehat{1-i}}). \end{cases} \tag{21}$$

Using notation (21), we then have

$$\begin{aligned} \mathcal{P}_i^* \mathcal{I}_{H_i^t} \mathcal{F}_i^t(x) &= \left[\mathcal{I}_{H_i^t} \mathcal{F}_i^t \right](x_{\widehat{1-i}}) \\ &= \mathcal{I}_{H^t} \left[\mathcal{F}_i^t(x_{\widehat{1-i}}) \right] \\ &= \mathcal{I}_{H^t} \left[\sum_{y \in \bar{H}} w(x_{\widehat{1-i}}, y_{\widehat{1-i}}) \left(\mathcal{P}_i \boldsymbol{f}^t(x_{\widehat{1-i}}) - \mathcal{P}_i \boldsymbol{f}^t(y_{\widehat{1-i}}) \right) \right] \\ &= \mathcal{I}_{H^t} \left[\sum_{y \in \bar{H}} w(x_{\widehat{1-i}}, y_{\widehat{1-i}}) \left(\boldsymbol{f}^t(x) - \boldsymbol{f}^t(y) \right) \right] \end{aligned} \tag{22}$$

and

$$\begin{aligned} \mathcal{P}_i^* \mathcal{G}_i^t(x) &= \mathcal{G}_i^t(x_{\widehat{1-i}}) \\ &= \sum_{y \in \bar{H}} 2w(x_{\widehat{1-i}}, y_{\widehat{1-i}}) \left(\mathcal{P}_i \boldsymbol{f}^t(x_{\widehat{1-i}}) - \mathcal{P}_i \boldsymbol{f}^t(y_{\widehat{1-i}}) \right) \\ &\quad + \mu \sum_{y \in H^t} 2w(x_{\widehat{1-i}}, y_{\widehat{1-i}}) \left(\mathcal{P}_i \boldsymbol{f}^t(x_{\widehat{1-i}}) - \mathcal{P}_i \boldsymbol{f}^t(y_{\widehat{1-i}}) \right) \\ &= \sum_{y \in \bar{H}} 2w(x_{\widehat{1-i}}, y_{\widehat{1-i}}) \left(\boldsymbol{f}^t(x) - \boldsymbol{f}^t(y) \right) \\ &\quad + \mu \sum_{y \in H^t} w(x_{\widehat{1-i}}, y_{\widehat{1-i}}) \left(\boldsymbol{f}^t(x) - \boldsymbol{f}^t(y) \right) \end{aligned} \tag{23}$$

and

$$\begin{aligned} \mathcal{P}_i^* GL^T \cdot D \cdot GL(x) &= \left[GL^T \cdot D \cdot GL \right](x_{\widehat{1-i}}) \\ &= \sum_{y \in \bar{H}} d_i \cdot w^2(x_{\widehat{1-i}}, y_{\widehat{1-i}}) \left(\mathcal{P}_i \boldsymbol{f}^t(x_{\widehat{1-i}}) - \mathcal{P}_i \boldsymbol{f}^t(y_{\widehat{1-i}}) \right) \\ &= \sum_{y \in \bar{H}} d_i \cdot w^2(x_{\widehat{1-i}}, y_{\widehat{1-i}}) \left(\boldsymbol{f}^t(x) - \boldsymbol{f}^t(y) \right) \\ &= GL^T \cdot D \cdot GL \boldsymbol{f}^t. \end{aligned} \tag{24}$$

By assembling weight matrices $w(x_{\widehat{1-i}}, y_{\widehat{1-i}})$ into

$$\bar{w}(x,y) = \sum_{i=1}^{d_s} w(x_{\widehat{1-i}}, y_{\widehat{1-i}}). \tag{25}$$

Then, (18) would be equivalent to the following:

$$\begin{aligned} &\sum_{y \in \bar{H}} 2\bar{w}(x,y) \left(\boldsymbol{f}^t(x) - \boldsymbol{f}^t(y) \right) \\ &\quad + \mu \sum_{y \in H^t} \bar{w}(x,y) \left(\boldsymbol{f}^t(x) - \boldsymbol{f}^t(y) \right) \\ &\quad + \mu \mathcal{I}_{H^t} \left[\sum_{y \in \bar{H}} \bar{w}(x,y) \left(\boldsymbol{f}^t(x) - \boldsymbol{f}^t(y) \right) \right] + \beta GL^T \cdot D \cdot GL \boldsymbol{f}^t \\ &\quad + \lambda \mathcal{I}_{H^t} \left(\boldsymbol{f}^t - \boldsymbol{b}^t \right) = 0, \forall x \in \bar{H}. \end{aligned} \tag{26}$$

Equation (26) is a sparse and linear system, where the third term is symmetric. However, the whole equation is asymmetric due to the projection operator $\mathcal{I}_{H^t}$. Thus, we choose the generalized minimal residual method (GMRES) to solve the system [34]. The optimization procedures for solving WNSR under the WNLL discretization framework is presented in Algorithm 1. For the nonweighted NSR model, we only need to replace the matrix D by the identity matrix $\boldsymbol{I}_{|C| \times |C|}$.

IV. EXPERIMENTAL RESULTS AND DISCUSSION

Experimental Settings: To evaluate our proposed WNSR method on HSI inpainting, in this section, we conduct extensive experiments using five well-known datasets, i.e., Pavia City Center, Washington DC Mall, Pavia University, RemoteImage, and Simu_Indian. In all experiments, four most recently proposed approaches are adopted as the competitors, including WNLL [28], TNN [14], total variation into low-rank tensor completion (LRTC-TV-II) [35], tensor train weighted optimization (TT-WOPT) [36]. WNLL is a patch-based method without considering second-order regularization. TNN takes the HSIs as tensor data and exploits low-rank property using a tubal rank. LRTC-TV-II introduces total variation (TV) term based on the low-rank constraint to strengthen the smoothness of spatial structure. TT-WOPT adopts an efficient tensor-train weighted decomposition to find the latent core tensors of the tensor data. All the experiments are conducted on the program platform with Intel Core i5-8250U 1.60 GHz and 8G RAM. The source code of our method has been uploaded online for evaluation. The website is https://github.com/ZhengJianwei2. Note that the main code of our algorithm is provided in an encrypted format, which will be decrypted after the review phase.

For all the competing methods, we follow the authors' suggestions to finetune the parameters guaranteeing the optimal results in all experiments. Unless otherwise specified, for WNSR, we limit the spatial patch size to 2×2 since the spatial resolution of the HSIs is often much lower than the natural RGB images. For each patch, the approximate nearest neighbor search algorithm and a k–d tree method are jointly used to efficiently obtain the nearest neighbors. The trade-off parameters λ and β are set as 1e8 and 0.05, respectively. The weight γ of semi-patch is set as 0.2. A more detailed discussion of settings would be shown in Section IV-B. Since that using a reasonable initialization would make WNSR easier to converge, we adopt the result of certain efficient algorithms, such as APG [37], as an initialization in our implementation.

Data Normalization: Let $\boldsymbol{b} \in \mathbf{R}^{m \times n \times B}$ denote the degraded hyperspectral data with B spectral bands and spatial size $m \times n$. We simply consider $\boldsymbol{b}$ as a collection of B 2-D images (or bands) with width m and height n. In our experiments, each band of the target HSI is normalized to the range of [0, 1] by the following formula:

$$\bar{\boldsymbol{b}}_h = \frac{\boldsymbol{b}_h - \min(\boldsymbol{b}_h)}{\max(\boldsymbol{b}_h) - \min(\boldsymbol{b}_h)}, h = 1, 2, \ldots, B \tag{27}$$

where $\boldsymbol{b}_h$ is the hth spectral band of $\boldsymbol{b}$, $\min(\boldsymbol{b}_h)$ and $\max(\boldsymbol{b}_h)$ respectively represent the minimum and maximum values of

---

Algorithm 1: (W)NSR for HSI Reconstruction.

Requirement: An incomplete observation HSI data $\boldsymbol{b}$ of an unknown HSI data $\boldsymbol{f} \in \mathbf{R}^{m \times n \times B}$. For every $t \in [B]$, $\boldsymbol{f}$ is partially observed on the subset H^t of $\bar{H} \in [m] \times [n]$. $\gamma = 0.2$, $\beta = 0.05$, $\lambda = 1e8$, $\mu = \frac{|\bar{H}^t|}{|H^t|} - 1$.

Output: A recovered HSI $\boldsymbol{f}$

Initialize $\boldsymbol{f}^{(t)}$, $t = 0$, as an $m \times n$ matrix by holding the known parts of $\boldsymbol{f}^t$ and filling the unknown parts randomly. For easier convergence, $\boldsymbol{f}^{(t)}$ can also be initialized by other fast implementation such as the APG algorithm [37].

while not converge **do**

  1. Generate the patch set $\mathcal{P}\boldsymbol{f}^{(k)}$ and get corresponding known set H^t.

  2. Get the matrix $D = diag\{d_1, d_2, \ldots, d_{|\bar{H}|}\}$ with $d_j = 1$ for $x_j \in \bar{H}^t \backslash H^t$ and $d_j = \frac{|\bar{H}^t|}{|H^t|}$ for $x_j \in H^t$.

  3. Compute the weight matrix on the spatial domain: $w(x, y) = w(\mathcal{P}\boldsymbol{f}^{(k)}(x), \mathcal{P}\boldsymbol{f}^{(k)}(y))$, $x, y \in \bar{H}$.

  4. Get the new assembled weight matrix and the graph Laplacian GL: $\bar{w}(x, y) = \sum_{i=1}^{d_s} w(x_{\widehat{1-i}}, y_{\widehat{1-i}})$.

  5. For every band t, get $(\boldsymbol{f}^t)^{(k+1)}$ by using GMRES to solve (26).

  6. $k \leftarrow k+1$.

end while

  $\boldsymbol{f} = \boldsymbol{f}^{(k)}$.

---

the pixels in $\boldsymbol{b}_h$. After restoration, the images with their original scale can be simply obtained as follows:

$$\bar{\boldsymbol{f}}_h = \boldsymbol{f}_h * (\max(\boldsymbol{b}_h) - \min(\boldsymbol{b}_h)) + \min(\boldsymbol{b}_h) \qquad (28)$$

where $\boldsymbol{f}_h$ is the learned image. Note that it has been reported in [6] that normalization and its inverse operation may cause some distortions. To investigate this phenomenon, we first randomly sample 5% pixels from Washington DC Mall, and then compare the recovered spectral signature to the original one using WNSR with and without normalization step. The results are shown in Fig. 2, where (30,180) is the selected missing point and mean DN denotes the average value of all pixel points. Moreover, the PSNR results of our method with or without normalization step are 41.78 and 42.77, respectively.

In Fig. 2(a) and (b), although partial pixel values of two recovered curves slightly deviate from the original ones, the mean DNs of the two recovered curves stick completely to the original spectral signature. In Fig. 2(c) and (d), both the results generated from WNSR with or without normalization step hold clear texture details. These observations demonstrate that normalization only leads to trivial influence on our method when applied in HSI inpainting problems. The practical reason for our adoption of this step is attributed to the fact that most algorithms [14], [35] report their results using numerical range [0, 1]. We try to present the results in similar circumstance and provide a fair comparison.
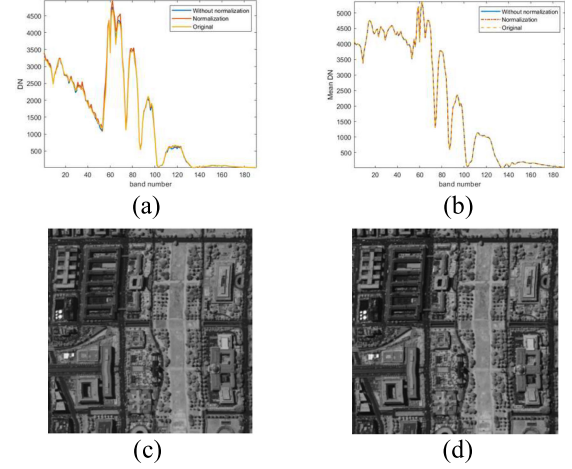

Fig. 2. Spectral signature and visual results (band 60) on Washington DC Mall under 95% random missing rate. (a) Pixel point (30,180), (b) Mean DN, (c) normalized and, (d) un-normalized.

A. WNSR for HSI Inpainting

To simulate the incomplete data, we randomly add missing pixels, Gaussian noise, and stripes to all the bands of five HSI datasets. Three kinds of cases are considered to investigate the performance of all competing methods, both visually and quantitatively. Detailed cases are listed as follows.

Case 1: Five different missing rates (MRs), i.e., 75%, 80%, 85%, 90%, 95%, are applied to each noisy-free HSI band independently.

Case 2: Based on 85% Gaussion missing rate, 20 row and column stripes with width 1 are further randomly distributed in each noisy-free HSI band. Moreover, certain thick deadlines with width 20 or 10 are added to bands 30–50 (case 2.1) or all bands (case 2.2).

Case 3: The Gaussian noise with variance 0.02 and random missing ratio 95% are imposed. In addition, 20 column stripes with width 1 are added to all bands.

1) Visual Quality Comparison: Following [29], we take the Simu_Indian data to show the results of case 1. This data contains 224 spectral bands with 145×145 spatial pixels in each band. By conducting case 1 with Simu_Indian, we illustrate the visual results of all competitors in Fig. 3 using different bands, where we mark certain region by a green box and enlarge it in red box for more detail's exhibition. From Fig. 3, several observations can be easily derived. First, most of the competing methods work effectively for HSI recovery from slight pixels missing. Second, TNN, LRTC-TV-II, and TTWOPT fail to deliver good results under high MRs, especially when the missing rate is at 90% or 95%. The reason may be partially attributed to the impact of Gaussian distribution of missing pixels, which poses difficulties in accurately estimating the intrinsic rank. Moreover, the results from LRTC-TV-II are over smooth because of the TV regularization that reduces the edge sharpness and texture details. Third, our WNSR performs best among all the competing approaches. Evidently, it can fill in the missing pixels more effectively, while preserving clearly the structure of the original
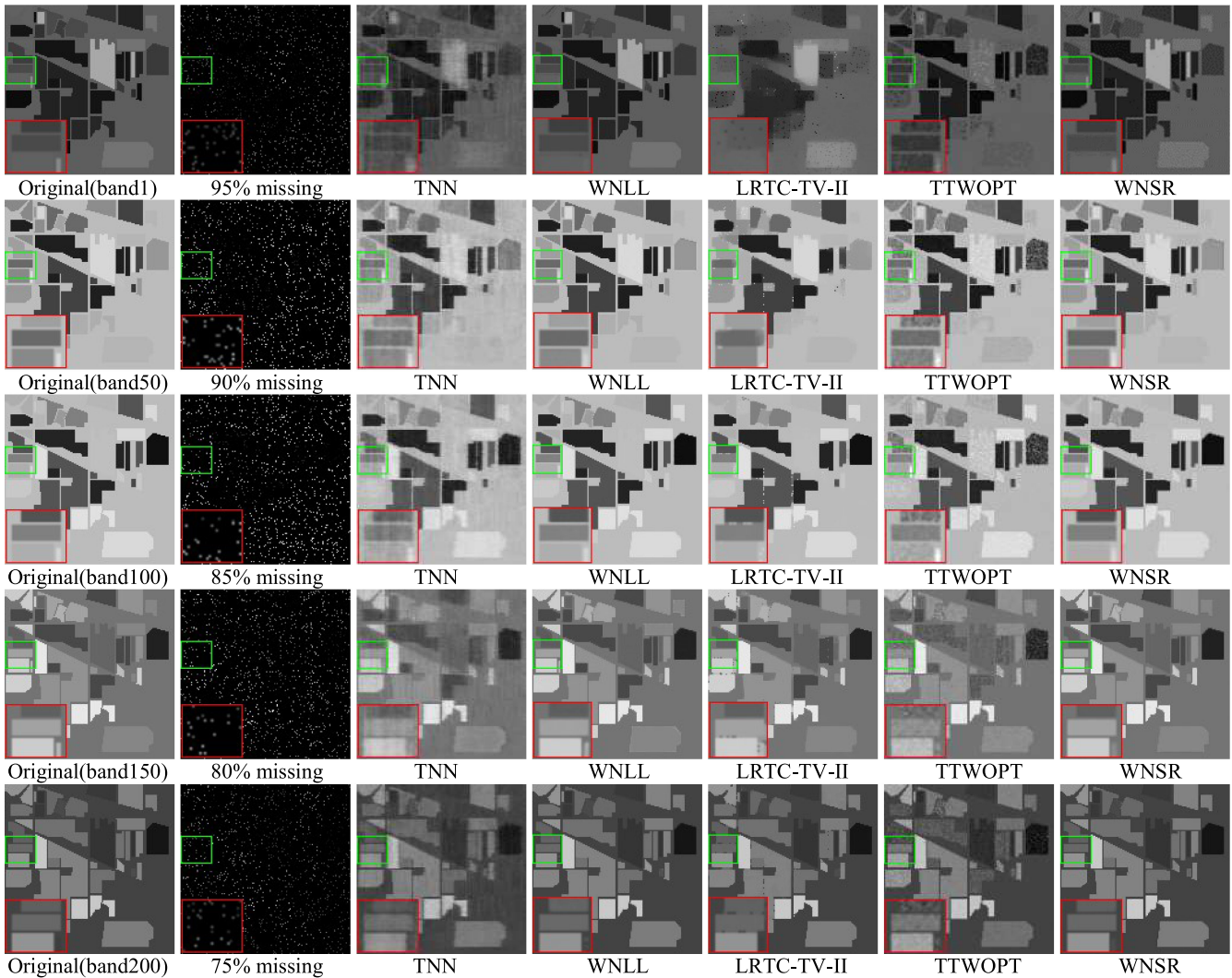
Fig. 3.   Restoration results of Simu_Indian data with different missing rates (75% to 95%).

HSI data. Although WNLL also achieves high visual quality, especially when the MRs are lower than 85%, its recovery results are evidently blurrier than ours. For instance, in the case with missing rate 75%, our WNSR method clearly preserves sharper edges and smoother patches than WNLL.

As introduced in [38], for most real situations, HSIs are corrupted by stripes and deadlines. In order to present direct comparison under these scenarios, we also add some random stripes and Gaussian noise to the original HSIs in case 2 and case 3. Figs. 4, 5, and 6 give the restoration results of case 2 and case 3 in Pavia city center (band 45), Simu_indian (band 10) and Pavia University (band 60), respectively. Note in Figs. 4 and 5, we do not illustrate the Gaussian missing pixels for the purpose of highlighting the distribution of stripes and deadlines.

Figs. 4 and 5 respectively show the recovered images with regarding to case 2.1 and case 2.2. In Fig. 4, LRTC-TV-II fails in inpainting the thick deadlines. This is attributed to the TV constraint that considers inner line pixels as positive property with local continuity. The remaining methods, i.e.,

TNN, WNLL, TTWOPT, and WNSR, all roughly recover the complete images. Comparatively, the recovered image from WNSR is much closer to the original one. From Fig. 5, our first observation is that most pinstripes can be well recovered by all competing methods. However, all methods fail in filling precise values into the pixels for thick deadline. Note this is the extreme case since our inpainting task is conducted in singleton scenarios, little information can be drawn due to the missing pixels from all bands. Among all the selected competitors, by comparatively looking into the details on the lower right corner, we can still find that the results from WNSR are smoother than those from others. The PSNR values also confirm the visual results. Similarly, in Fig. 6, the restored images from the competing methods, i.e., TNN, WNLL, LRTV-TV-II, and TTWOPT, again are much noisy and blurry. Benefiting from the advantage of second-order regularizer, the recovered image of our WNSR method is relatively smoother than others. Unfortunately, for the same reason of seeking smooth results, certain sharp edges of images generated from WNSR are compromised. Specifically, one can see that in the top right corner of Fig. 6, a bright pixel
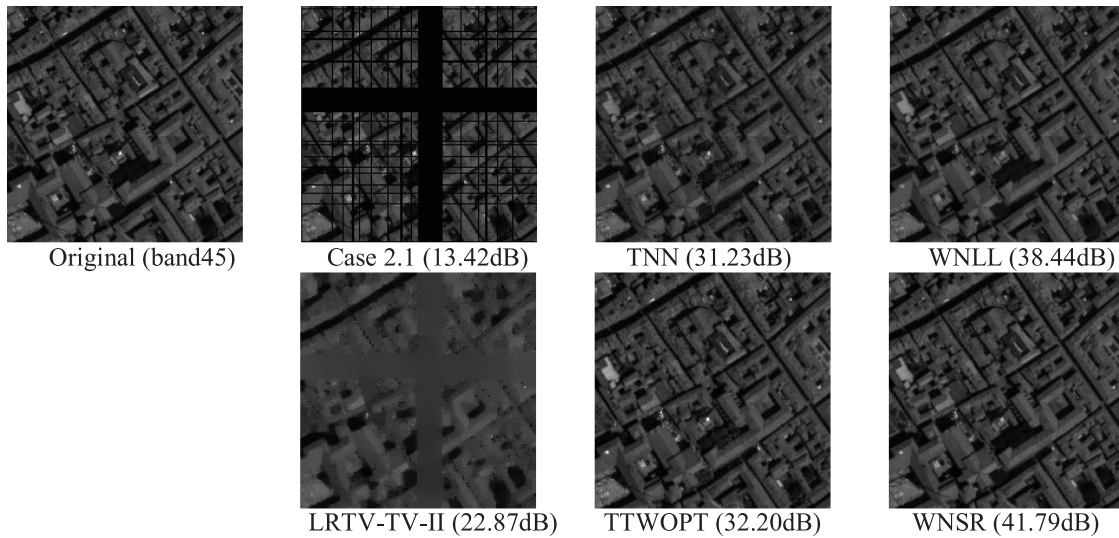
Original (band45) Case 2.1 (13.42dB) TNN (31.23dB) WNLL (38.44dB)

LRTV-TV-II (22.87dB) TTWOPT (32.20dB) WNSR (41.79dB)

Fig. 4. Restoration results of Case 2.1 (with two thick deadlines in bands 30–50) on Pavia City Center data.

Original (band10) Case 2.1 (15.57dB) TNN (30.78dB) WNLL (30.53dB)

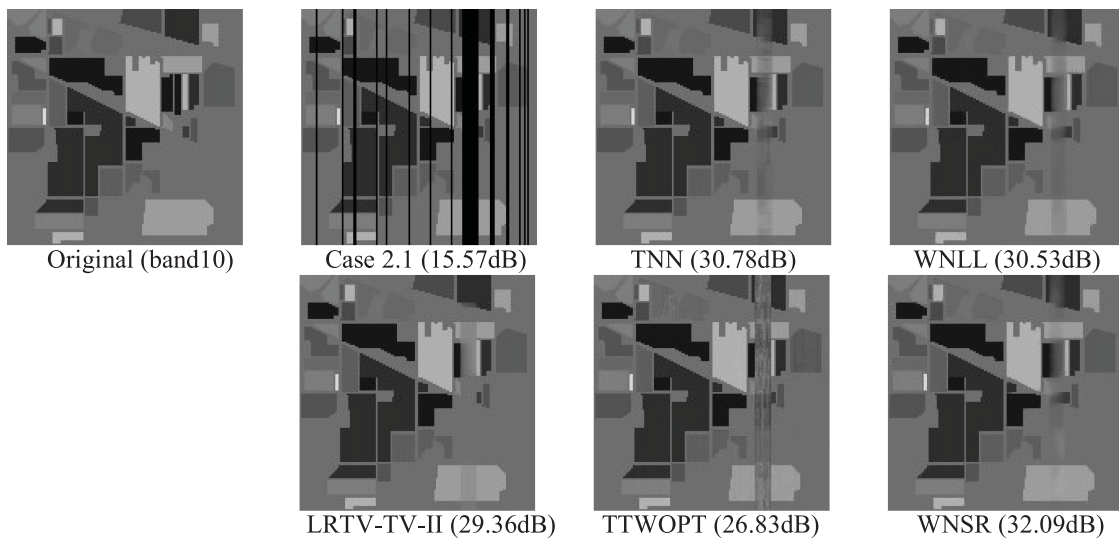LRTV-TV-II (29.36dB) TTWOPT (26.83dB) WNSR (32.09dB)

Fig. 5. Restoration results of Case 2.2 (with a thick deadline in all bands) on Simu_Indian data.

is mistakenly removed by WNSR. Nonetheless, we believe that this imperfection is acceptable since WNSR behaves desirably in most cases. From another point of view, this characteristic also holds the potential for some other applications, such as anomaly detection [39]. Overall, from all these three figures, we can observe that WNSR restores images with high fidelity of visual quality in different inpainting scenarios, which preserves much delicate details of the original images.

2) Quantitative Comparison: In this part, three well-known numerical indicators are adopted to give a quantitative assessment, including mean peak signal-to-noise ratio (MPSNR) and structural similarity (MSSIM). In order to objectively evaluate the spectral fidelity of the recovered results, the mean spectral angle (MSA) [40] is also used. Table I lists the results by applying different methods in Washington DC Mall, where the

best numerical values are shown in bold face. Again, it is evident that the proposed WNSR algorithm performs best on average in all three cases. Although TNN performs slightly better than our method under 75% missing rate, its performance in other cases is poorer than ours. For all the three cases of the Washington DC Mall image, the average improvement of WNSR over TNN is 1.27, 0.023, and 0.84 in terms of MPSNR, MSSIM, and MSA, respectively. Note that case 3 is undoubtedly the most difficult scenario. Encouragingly, we can observe that our proposed WNSR enjoys a definitely superior performance over the other competitors.

In addition, Fig. 7 shows the curves of MPSNR, MSSIM, and MSA values against five missing rates in Case 1. Our first observation is that the curves of MPSNR and MSSIM maintain a downward trend, while the results of MSA keep increasing
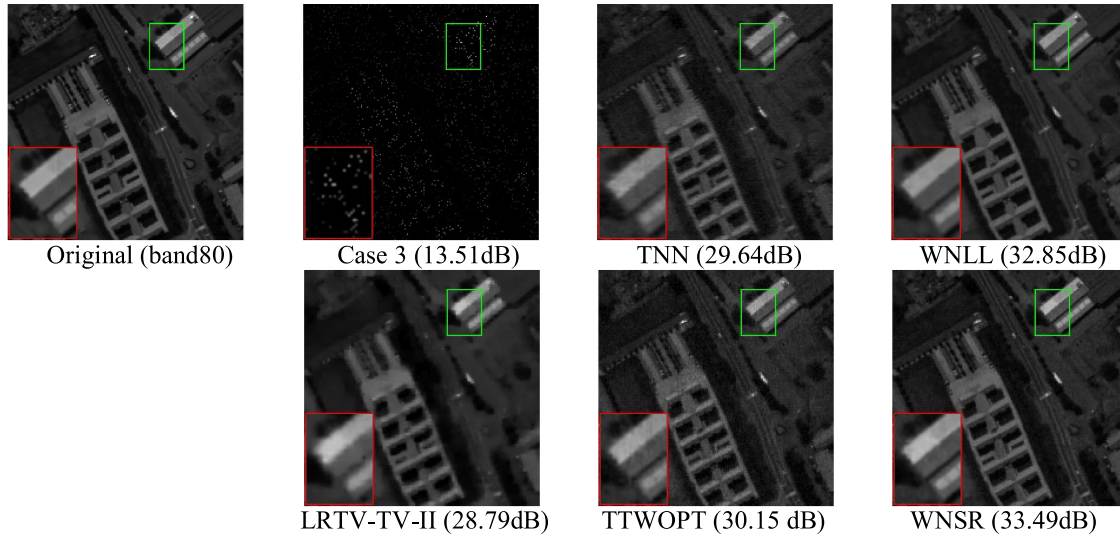
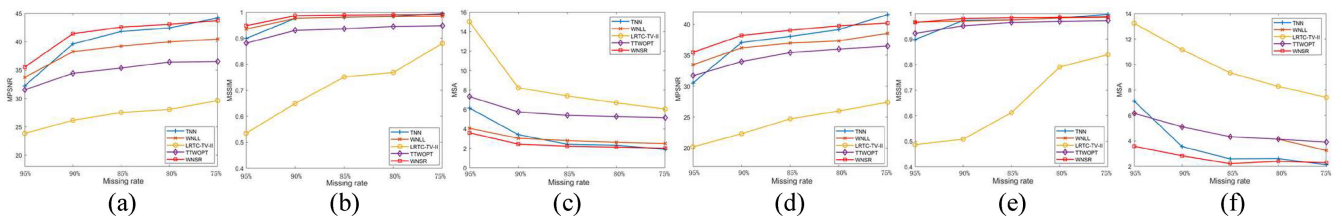Fig. 6. Restoration results of Case 3 on Pavia University data.

Fig. 7. MPSNR, MSSIM, and MSA values of Pavia city center (a)–(c) and Washington DC Mall (d)–(f) under case1 generated by TNN, WNLL, LRTC-TV-II, TTWOPT, and WNSR, respectively.
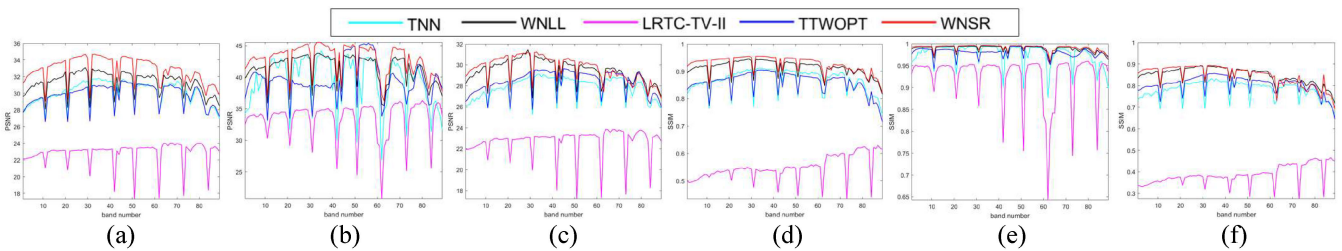

Fig. 8. Detailed quantitative evaluation of competing approaches for each band on RemoteImage. (a), (b) Case 1, (c), (d) Case 2.1, (e), and (f) Case 3.

along with the higher MR values. This is reasonable since a higher sampling rate always means more useful information would be available. We can also see that our WNSR achieves the best numerical values compared to others when MR is equal or higher than 80%. Note that when missing rate equals 75%, most of the algorithms work quite effectively, and the difference of their best numerical values are insignificant. To better illustrate the stability of different algorithms, Fig. 8 shows the PSNR and SSIM values of each band on RemoteImage, where the horizontal axis in the figure represents the band number, and the vertical axis represents the PSNR or SSIM result in that band. In this figure, WNSR again achieves the best performance almost in all the bands. Fig. 9 further shows the behavior of

spectral consistency on representative pixels. It is evident that the profiles generated from TNN, LRTC-TV-II, and TTWOPT deviate far from the original ones. WNLL and WNSR both can capture the main spectral consistency. From a deeper insight, the curves of our method are more natural and much closer to the original one, which again demonstrates the superiority of our second-order constraint.

3) Running Time Comparison: Taking case 1 as an example, Table II lists the runtime of all methods on RemoteImage data.

Similarly, Fig. 10 illustrates the execution time of all the competing methods on Simu_Indian data. In both Fig. 10 and Table II, the efficiency of our method is very competitive compared to others. Note that the performance of WNSR ranks first

TABLE I
COMPARISON RESULTS OF DIFFERENT METHODS IN CASES 1–3 ON WASHINGTON DC MALL

| Data	Cases	MRs(%)	index	corrupted image	TNN	WNLL	LRTC-TV-II	TTWOPT	WNSR
Washington DC Mall image	Case 1	95	MPSNR(dB)	12.45	30.51	33.45	20.18	31.69	**35.47**
			MSSIM	0.010	0.898	0.952	0.487	0.922	**0.965**
			MSA(rad)	77.51	7.12	4.29	13.23	6.16	**3.57**
		90	MPSNR(dB)	12.68	37.05	36.18	22.31	33.97	**38.18**
			MSSIM	0.026	0.973	0.970	0.508	0.952	**0.980**
			MSA(rad)	71.83	3.54	3.47	11.15	5.10	**2.84**
		85	MPSNR(dB)	12.93	38.03	36.95	24.37	35.42	**39.03**
			MSSIM	0.05	0.972	0.974	0.612	0.965	**0.983**
			MSA(rad)	67.39	2.68	3.21	9.34	4.32	**2.59**
		80	MPSNR(dB)	13.19	39.14	36.92	25.99	35.98	**39.74**
			MSSIM	0.07	0.982	0.974	0.7991	0.969	**0.985**
			MSA(rad)	63.59	2.43	3.22	8.28	4.14	**2.41**
		75	MPSNR(dB)	13.48	**41.54**	37.52	27.40	36.48	40.19
			MSSIM	0.10	**0.997**	0.977	0.839	0.972	0.987
			MSA(rad)	60.11	**2.12**	3.04	7.41	3.90	2.28
	Case 2.1	85	MPSNR(dB)	16.78	29.07	42.23	35.42	30.19	**43.77**
			MSSIM	0.386	0.865	0.991	0.964	0.894	**0.996**
			MSA(rad)	36.56	1.66	1.92	4.08	2.64	**1.59**
	Case 2.2	85	MPSNR(dB)	17.38	32.14	31.63	30.91	28.99	**32.48**
			MSSIM	0.496	0.954	0.955	0.951	0.948	**0.962**
			MSA(rad)	34.38	2.49	3.64	3.05	2.58	**2.03**
	Case 3	95	MPSNR(dB)	12.43	27.75	31.97	19.87	30.49	**32.38**
			MSSIM	0.008	0.818	0.932	0.442	0.896	**0.918**
			MSA(rad)	78.41	9.03	6.44	13.64	7.12	**6.30**

| TNN | WNLL | LRTC-TV-II | TTWOPT | WNSR |
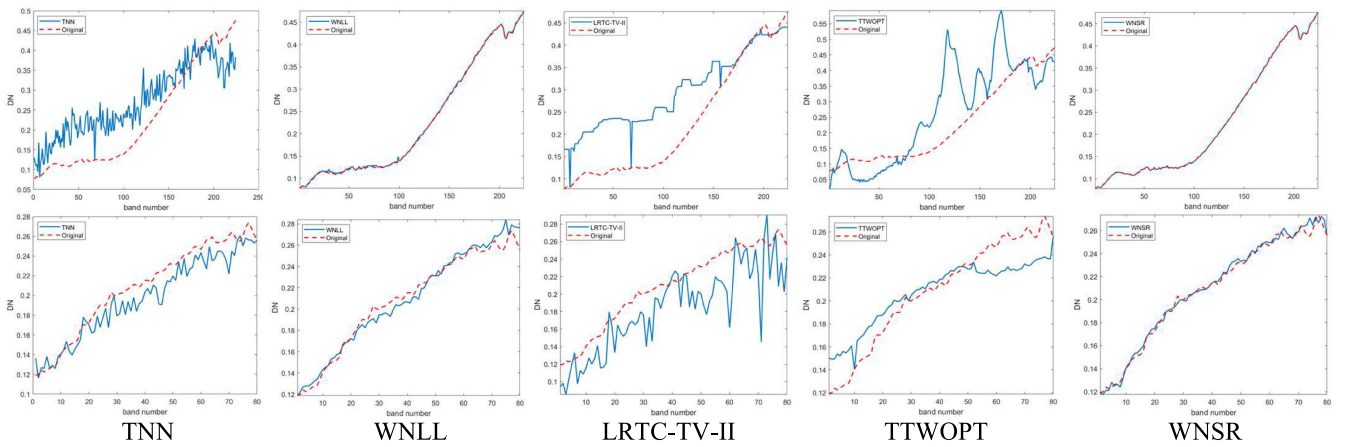
Fig. 9. Spectrum of pixel (75,75) in Simu_Indian center (top row) and pixel (150,150) in Pavia city (bottom row) under 95% random missing rate.

in almost all the aforementioned experimental results. WNLL is the most efficient approach among all the five algorithms due to its usage of simpler constraint. Accordingly, its performance is inferior to WNSR both quantitatively and visually. TNN, LRTC-TV-II, and TTWOPT are tensor decomposition-based methods, which is time-consuming at finding the latent core tensor rank. For LRTC-TV-II, a step for computing the inverse

of a matrix is unavoidably required in each iteration, which further increases the running time. The reasonable efficiency of WNSR while holding the best visual quality stems from the weight assembly step, which combines $s_1 \times s_2$ equations in the spatial domain into only one equation. Furthermore, adopting the semi-patch technique can also slightly improve the efficiency of WNSR with the sacrifice of recovery performance

TABLE II
RUNTIME OF ALL THE FIVE METHODS ON REMOTE IMAGE WITH
MRS FROM 75% TO 95% IN CASE1

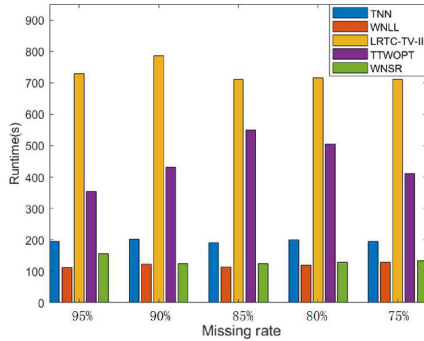| MRs(%)	TNN	WNLL	LRTC-TV-II	TTWOPT	WNSR
95	109.0s	75.7s	633.9s	120.2s	104.4s
90	109.1s	63.1s	570.7s	179.3s	72.4s
85	107.9s	81.2s	593.8s	186.1s	69.3s
80	117.1s	74.4s	604.2s	200.2s	96.7s
75	115.2s	81.2s	613.2s	185.6s	102.5s

Fig. 10. Execution time of all competing methods under MRs 75%–95% on Simu_Indian data.
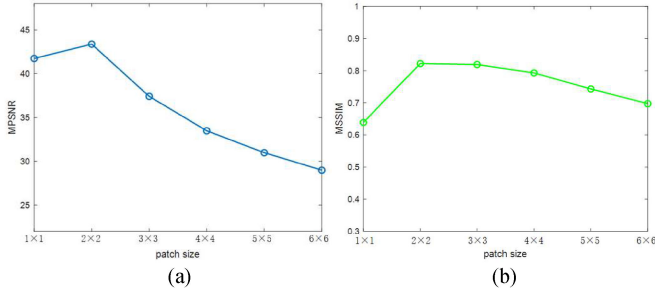

Fig. 11. Sensitivity analysis of patch size p_s in Simu_Indian. (a) MPSNR. (b) MSSIM.

in an acceptable range. More details can be found in the next section.

4) Parameters Discussion: In this section, sensitivity analysis of two essential parameters, i.e., patch size p_s and the weight parameters γ, are undertaken on the noisy-free Simu_Indian data in case 1 with missing rate 90%. All the results are averaged from ten trials.

1) *Patch size p_s:* By varying p_s from 1 to 6, the inpainting results in terms of MPSNR and MSSIM are shown in Fig. 11. We can observe that WNSR gets the best numerical performance. when p_s is set as 2. These results are reasonable since the spatial resolution of HSI is relatively small. A larger patch size would lead to a loose capture of detailed structure information.

On the contrary, directly using a single-pixel as the patch unit cannot utilize any spatial information. Therefore, patch size 2 is a suggested setting in practical usage of our method.

TABLE III
MPSNR VALUES OF DIFFERENT METHODS IN FIVE DATASETS WITH
MRS 95%, 90%, 85%, RESPECTIVELY

Methods	Pavia Center	WashingtonDC	Simu_Indian	RemoteImage
MR		95%		
GL	31.3153	30.0405	37.3098	28.4718
WNLL	34.2365	33.4667	40.3425	31.4754
NSR	33.6731	32.8850	39.7703	30.8972
WNSR	35.7228	35.1347	41.6349	32.9587
MR		90%		
GL	36.9894	34.1697	38.3633	33.1326
WNLL	38.8365	35.9573	41.1282	34.7480
NSR	38.9559	36.0638	41.3528	34.8750
WNSR	41.3375	38.1114	43.5013	37.0489
MR		85%		
GL	38.5095	35.5851	39.4820	34.7157
WNLL	39.7630	36.7153	42.1107	35.6190
NSR	40.1974	37.1688	42.6968	34.0400
WNSR	42.4135	39.0218	44.5775	37.9370

2) *Weight parameter γ of semi-patch:* Parameter γ is used to restrict the weight of local coordinate information. As shown in Fig. 12, with the increase of weight γ, the runtime of our method is gradually reduced. Meanwhile, the MPSNR and MSSIM results are relatively stable when γ is smaller than 0.4. However, they turn into a decreasing trend when the parameter is larger than 0.4. These results together lead to a conclusion that with a proper selection of γ, the efficiency of WNSR would be improved with a little sacrifice of the recovery performance.

B. Component Analysis for WNSR

Under the assumption that the image patches lie on a low dimension and smooth manifold, in this experiment, we directly compare the performance difference among several variants of WNSR, including GL, WNLL and NSR. Among them, WNLL and GL only adopt the first-order and second-order regularization, respectively. NSR is the nonweighted version of WNSR.

All these methods aim to reconstruct HSI images using the low-dimensional property. The conjugate gradient method is used to solve the linear system in weighted nonlocal Laplacian and graph Laplacian. All the experiment settings of WNSR are as same as in previous experiments.

The numerical results are shown in Tables III and IV, where the best and second best results are highlighted in bold face and with underline, respectively. It is clear from these tables that our WNSR algorithm significantly improves the recovery accuracy in all datasets. We can observe that WNLL performs worse than NSR when MR is lower than 90% and performs better when MR reaches 95%. It is reasonable because when the MR is high, WNLL can provide more balanced prior information than NSR. On the contrary, when there are enough known pixels, NSR can make more use of the intrinsic smoothness characteristics of the image. Considering the loss rate of real-life HSIs, we believe that NSR is more suitable for practical situations than WNLL. Fig. 13 provides a visual illustration of these results. What is easy to find from the error map is that our WNSR keeps both the smoothness and the edge information better than the compared method.
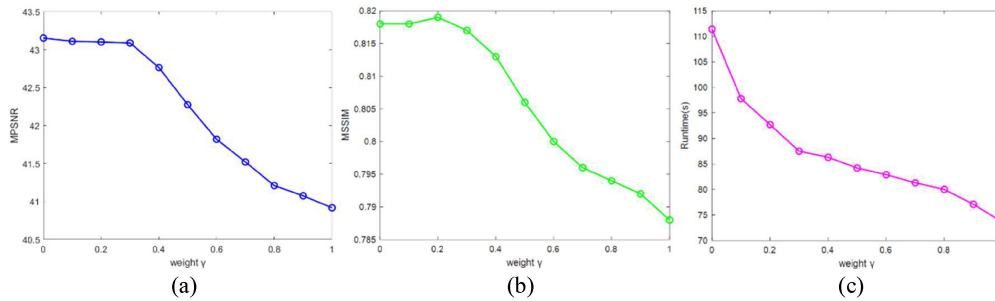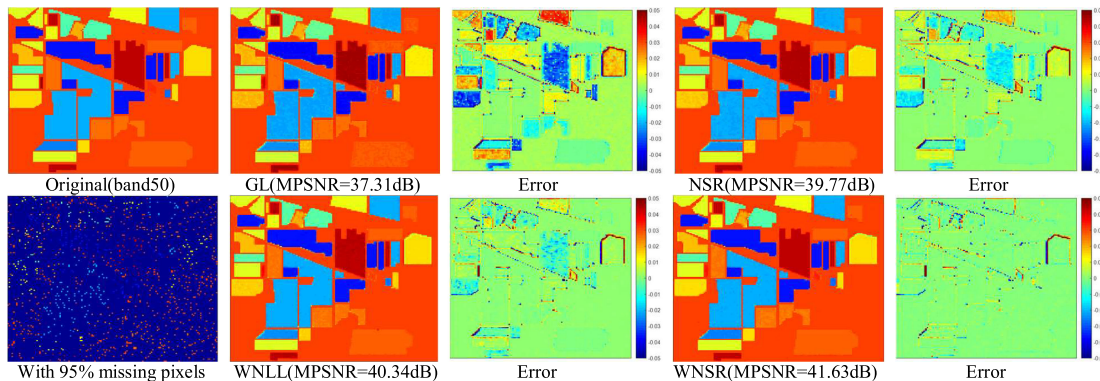
Fig. 12. MPSNR, MSSIM, and runtime results of Simu_Indian data under increasing γ. (a) MPSNR. (b) MSSIM. (c) Runtime(s).

Original(band50) GL(MPSNR=37.31dB) Error NSR(MPSNR=39.77dB) Error

With 95% missing pixels WNLL(MPSNR=40.34dB) Error WNSR(MPSNR=41.63dB) Error

Fig. 13. Reconstruction of the Simu_Indian dataset from 95% pixels missing. The error is presented with a scale of 1/20 to highlight the difference.

TABLE IV
MPSSIM Values of Different Methods in Five Datasets With MRs 95%, 90%, 85%, Respectively

| Methods	Pavia Center	WashingtonDC	Simu_Indian	RemoteImage
MR		95%		
GL	0.9049	0.9116	0.6665	0.8090
WNLL	0.9400	0.9520	0.7544	0.8762
NSR	0.9344	0.9472	0.7404	0.8668
WNSR	**0.9520**	**0.9648**	**0.8111**	**0.8987**
MR		90%		
GL	0.8741	0.9680	0.9569	0.6828
WNLL	0.8949	0.9780	0.9695	0.7434
NSR	0.8991	0.9787	0.9702	0.7698
WNSR	**0.9119**	**0.9858**	**0.9799**	**0.8484**
MR		85%		
GL	0.8904	0.9766	0.9670	0.6910
WNLL	0.9059	0.9821	0.9736	0.7953
NSR	0.9105	0.9839	0.9759	0.8251
WNSR	**0.9192**	**0.9891**	**0.9832**	**0.8472**

V. CONCLUSION

In this article, we use both the low dimensionality and the smoothness of the patch manifold as the regularization terms for missing pixels recovery of the HSIs. Specifically, to better keep the smoothness, we introduce a nonlocal second-order regularization and a weighted version based on the typical LDMM constraint. In contrast to only using the property of low dimensionality alone, the joint consideration of both low dimensionality and smoothness can optimistically approximate the real manifold. The model is solved by a GMRES algorithm. Moreover, a semi-local patch technique is used to speed up the efficiency of our model. Various comparison experiments with several most recently published algorithms demonstrate the superiority of our proposed constraint. In the near future, we are interested in extending our method to the subspace coefficients of HSI, which would further enhance the efficiency for better practicability.

REFERENCES

[1] P. Ghamisi *et al.*, "Advances in hyperspectral image and signal processing: A comprehensive overview of the state-of-the-art," *IEEE Geosci. Remote Sens. Mag.*, vol. 5, no. 4, pp. 37–78, Dec. 2017.

[2] J. Zheng, Y. Feng, C. Bai, and J. Zhang, "Hyperspectral image classification using mixed convolutions and covariance pooling," *IEEE Trans. Geosci. Remote Sens.*, to be published, doi: 10.1109/TGRS.2020.2995575.

[3] Y. Yuan, J. Lin, and Q. Wang, "Hyperspectral image classification via multitask joint sparse representation and stepwise MRF optimization," *IEEE Trans. Cybern.*, vol. 46, no. 12, pp. 2966–977, Dec. 2016.

[4] X. Song and L. Wu, "Hyperspectral image inpainting based on robust spectral dictionary learning," *Appl. Sci.*, vol. 9, no. 15, 2019, Art. no. 3062.

[5] L. G. S. Nie, Y. Zheng, A. Lam, and N. Ono, "Deeply learned filter response functions for hyperspectral reconstruction," in *Proc. IEEE/CVF Conf. Comput. Vis. Pattern Recognit.*, 2018, pp. 4767–4776.

[6] Y. Li, W. Xie, and H. Li, "Hyperspectral image reconstruction by deep convolutional neural network for classification," *Pattern Recognit.*, vol. 63, pp. 371–383, 2017.

[7] X. Y. X. Miao, Y. Pu, and V. Athitsos, "Lambda-Net: Reconstruct hyperspectral images from a snapshot measurement," in *Proc. IEEE/CVF Int. Conf. Comput. Vis.*, 2019, pp. 4058–4068.

[8] P. H. A. *et al.*, "Low-rank nonnegative matrix factorization on stiefel manifold," *Inf. Sci.*, vol. 514, pp. 131–148, 2020.

[9] F. Xiong, Y. Qian, J. Zhou, and Y. Y. Tang, "Hyperspectral unmixing via total variation regularized nonnegative tensor factorization," *IEEE Trans. Geosci. Remote Sens.*, vol. 57, no. 4, pp. 2341–2357, Apr. 2019.

[10] J. W. Zheng, P. Yang, X. Yang, and S. Y. Chen, "Truncated low-rank and to-tal p variation constrained color image completion and its Moreau approx-imation algorithm," *IEEE Trans. Image Process.*, vol. 29, pp. 7861–7874, 2020, doi: 10.1109/TIP.2020.3008367.

[11] T. Y. Ji *et al.*, "A non-convex tensor rank approximation for tensor completion," *Appl. Math. Model.*, vol. 48, pp. 410–422, 2017.

[12] T. X. Jiang *et al.*, "Matrix factorization for low-rank tensor completion using framelet prior," *Inf. Sci.*, vol. 436–437, pp. 403–417, 2018.

[13] C. Lu, J. Feng, Y. Chen, W. Liu, Z. Lin, and S. Yan, "Tensor robust principal component analysis with a new tensor nuclear norm," *IEEE Trans. Pattern Anal. Mach. Intell.*, vol. 42, no. 4, pp. 925–938, Apr. 2020.

[14] C. Lu *et al.*, "Exact low tubal rank tensor recovery from gaussian mea-surements," in *Proc. Int. Joint Conf. Artif. Intell.*, 2018, pp. 2504–2510.

[15] Y. Chen, W. He, N. Yokoya, and T. -Z. Huang, "Hyperspectral image restoration using weighted group sparsity-regularized low-rank tensor decomposition," *IEEE Trans. Cybern.*, vol. 50, no. 8, pp. 3556–3570, Aug. 2020.

[16] X. Bai, F. Xu, L. Zhou, Y. Xing, L. Bai, and J. Zhou, "Nonlocal similarity based nonnegative tucker decomposition for hyperspectral image denois-ing," *IEEE J. Sel. Top. Appl. Earth Observ. Remote Sens.*, vol. 11, no. 3, pp. 701–712, Mar. 2018.

[17] R. Dian, S. Li, and L. Fang, "Learning a low tensor-train rank representa-tion for hyperspectral image super-resolution," *IEEE Trans. Neural Netw.*, vol. 30, no. 9, pp. 2672–2683, Sep. 2019.

[18] Y. Chen, W. He, N. Yokoya, T. Huang, and X. Zhao, "Nonlocal tensor-ring decomposition for hyperspectral image denoising," *IEEE Trans. Geosci. Remote Sens.*, vol. 58, no. 2, pp. 1348–1362, Feb. 2020.

[19] Y. Wang, J. Peng, Q. Zhao, Y. Leung, X. Zhao, and D. Meng, "Hyper-spectral image restoration via total variation regularized low-rank tensor decomposition," *IEEE J. Sel. Top. Appl. Earth Observ. Remote Sens.*, vol. 11, no. 4, pp. 1227–1243, Apr. 2018.

[20] J. V. Manjón *et al.*, "Adaptive non-local means denoising of MR images with spatially varying noise levels," *J. Magn. Reson. Imag.*, vol. 31, no. 1, pp. 192–203, 2010.

[21] Q. Guo, S. Gao, X. Zhang, Y. Yin, and C. Zhang, "Patch-Based image in-painting via two-stage low rank approximation," *IEEE Trans. Vis. Comput. Graph.*, vol. 24, no. 6, pp. 2023–2036, Jun. 2018.

[22] G. Peyre, "Image processing with nonlocal spectral bases," *Multiscale Model. Simul.*, vol. 7, no. 2, pp. 703–730, 2008.

[23] G. Peyre, "A review of adaptive image representations," *IEEE J. Sel. Top. Signal Process.*, vol. 5, no. 5, pp. 896–911, Sep. 2011.

[24] R. Yin *et al.*, "A tale of two bases: Local-nonlocal regularization on image patches with convolution framelets," *Siam J. Imag. Sci.*, vol. 10, no. 2, pp. 711–750, 2017.

[25] X. Cheng, M. Rachh, and S. Steinerberger, "On the diffusion geometry of graph laplacians and applications," *Appl. Comput. Harmon. Anal.*, vol. 46, no. 3, pp. 674–688, 2019.

[26] Y. H. Yang, J. W. Zheng, S. Y. Chen, and M. Y. Zhang, "Hyperspec-tral image restoration via local low-rank matrix recovery and Moreau-enhanced total variation," *IEEE Geosci. Remote Sens. Lett.*, vol. 17, no. 6, pp. 1037–1041, Jun. 2020.

[27] S. Osher, Z. Shi, and W. Zhu, "Low dimensional manifold model for image processing," *Siam J. Imag. Sci.*, vol. 10, no. 4, pp. 1669–1690, 2017.

[28] Z. Shi, S. Osher, and W. Zhu, "Generalization of the weighted nonlocal laplacian in low dimensional manifold model," *J. Sci. Comput.*, vol. 75, no. 2, pp. 638–656, 2018.

[29] Z. Shi, W. Zhu, and S. Osher, "Low dimensional manifold model in hyperspectral image reconstruction," in *Hyperspectral Image Analysis*. New York, NY, USA: Springer, 2020.

[30] T. Lu, W. Liu, and Z. Pan, "Color image restoration and inpainting via multi-channel total curvature," *Appl. Math. Model.*, vol. 61, pp. 280–299, 2018.

[31] B. Jiang, C. Ding, J. Tang, and B. Luo, "Image representation and learning with graph-laplacian tucker tensor decomposition," *IEEE Trans. Cybern.*, vol. 49, no. 4, pp. 1417–1426, Apr. 2019.

[32] Z. Shi, S. Osher, and W. Zhu, "Weighted nonlocal laplacian on interpola-tion from sparse data," *J. Sci. Comput.*, vol. 73, no. 2-3, pp. 1164–1177, 2017.

[33] A. Spira, R. Kimmel, and N. Sochen, "A Short- Time Beltrami kernel for smoothing images and manifolds," *IEEE Trans. Image Process.*, vol. 16, no. 6, pp. 1628–1636, Jun. 2007.

[34] S. Gazzola and M. S. Landman, "Flexible GMRES for total variation regularization," *Bit. Numer. Math.*, vol. 59, pp. 721–746, 2019.

[35] X. Li, Y. Ye, and X. Xu, "Low-rank tensor completion with total variation for visual data inpainting," in *Proc. 31st AAAI Conf. Artif. Intell.*, 2017, pp. 2210–2216.

[36] Z. Q. Yuan and J. Cao, "Completion of high order tensor data with missing entries via tensor-train decomposition," in *Proc. Int. Conf. Neural Inf. Process.*, 2017, pp. 222–229.

[37] K. C. Toh and S. Yun, "An accelerated proximal gradient algorithm for nuclear norm regularized least squares problems," *Pac. J. Optim.*, vol. 6, no. 3, pp. 615–640, 2010.

[38] W. He, H. Zhang, L. Zhang, and H. Shen, "Total-variation-regularized low-rank matrix factorization for hyperspectral image restoration," *IEEE Trans. Geosci. Remote Sens.*, vol. 54, no. 1, pp. 178–188, Jan. 2016.

[39] N. Huyan, X. Zhang, H. Zhou, and L. Jiao, "Hyperspectral anomaly detection via background and potential anomaly dictionaries construc-tion," *IEEE Trans. Geosci. Remote Sens.*, vol. 57, no. 4, pp. 2263–2276, Apr. 2019.

[40] X. Z. Li *et al.*, "HSVCNN: CNN-based hyperspectral reconstruction from RGB videos," in *Proc. 25th IEEE Int. Conf. Image Process.*, 2018, pp. 3323–3327.
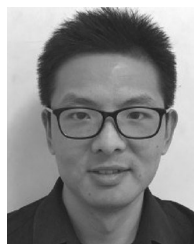
Jianwei Zheng received the B.S. degree in electronic and computer engineering and the Ph.D. degree in control theory and control engineering from the Zhejiang University of Technology, Hangzhou, China, in 2005 and 2010, respectively.

He is an Associate Professor with the College of Computer Science and Technology, Zhejiang Uni-versity of Technology. His research interests include machine learning and compressive sensing. He has authored more than 60 journal articles and conference papers in these areas.

Jiawei Jiang received the B.E degree from the China Jiliang University, Hangzhou, China, in 2018. He is currently working toward the M.S. degree with the College of Computer Science and Technology, Zhejiang University of Technology, Hangzhou.

His current research interests include remote-sensing image process and its application.

Honghui Xu received the B.E. degree from Zhejiang University of Technology, Hangzhou, China, in 2018. He is currently working toward the Ph.D. degree in the School of Computer Science and Engineering, Zhejiang University of Technology.

His current research interests include image pro-cessing and optimization algorithm.

Zhi Liu received the B.S. degree in automatic con-trol and the M.S. degree in system engineering from Xi'an Jiaotong University, Xi'an, China, in 1991 and 1994, respectively, and the Ph.D. degree in computer science and technology from Zhejiang University, Hangzhou, China, in 2001.

She is currently a Professor with the College of Computer Science and Technology, Zhejiang Univer-sity of Technology, Hangzhou. Her research interests mainly include 3-D model retrieval, image process-ing, and intelligent transportation system.

Fei Gao received the B.S. degree in mechanical en-gineering from the Zhejiang University, Hangzhou, China, in 1998, and the Ph.D. degree in mechanical engineering from Zhejiang University, Hangzhou, in 2004.

He has authored a book, more than 90 articles, and more than 70 inventions. His research interests include visual perception and understanding, pat-tern recognition, object tracking, and background modeling.